

Chapter 5

A compendium of rubidium scattering properties

The low-energy scattering properties of Rb in a magnetic trap are now well understood. This is a dramatic departure from the situation of just a few years ago. It has taken a number of experiments and corresponding theoretical analyses to provide a clear and consistent picture. Most notable among the early experiments were the observations of d -wave[101] and g -wave[102] shape resonances in scattering of doubly-polarized ^{87}Rb atoms and ^{85}Rb atoms, respectively. In both experiments, the observation of additional rotational lines in the photoassociation spectra signaled the presence of enhanced $l = 2$ or 4 ground state collisions. Cloud temperatures were in range of hundreds of μK range, well below the centrifugal barrier whereby collisions in these higher partial waves should have been suppressed. An analysis of the photoassociation lineshapes provided limits on both the triplet scattering length a_t and the leading order dispersion coefficient C_6 .

The singlet scattering length a_s was unknown until the experiment of Myatt, **et al.**[100], that obtained, surprisingly, a pair of Bose condensates coexisting in the same magnetic trap. Prior to this experiment it was generally expected that the two trapped spin-states ($|f_a, m_{f_a}\rangle \equiv |2, 2\rangle$ and $|1, -1\rangle$) would suffer huge spin-exchange losses, leading to the destruction of the mixed cloud before it could condense. The anomalous suppression of the spin-exchange loss rate signaled the near equivalence of the singlet and triplet scattering lengths, as was pointed out almost simultaneously by three groups[103, 104, 105]. The other novel aspect of this experiment was that only atoms in one spin-state ($|1, -1\rangle$) was evaporatively cooled. Atoms in the $|2, 2\rangle$ spin-state cooled sympathetically (i.e., through elastic collisions with the $|1, -1\rangle$ atoms). This provided a “proof-of-principle” for a new route to condensation that might be applied to other hard to cool species. For example, this might be useful for fermionic isotopes for which s -waves collisions between two atoms in the same spin-polarized state is forbidden. An analysis of the Myatt, **et al.** experiment will be the subject of Section 5.1.

The observation of a magnetically-induced Feshbach resonance by Roberts, **et al.**[17] has provided the most definitive bounds on the Rb interaction parameters (a_s , a_t , and C_6), to date. The same resonance had also been observed using photoassociation spectroscopy techniques[16] but uncertainties in the magnetic field

calibration and the difficulty of the corresponding theoretical analysis led to much larger uncertainties in the potential parameters extracted in Ref.[16]. An analysis of the Roberts, **et al.** experiment will be detailed in Section 5.2.

These experiments, coupled with our theoretical analysis, have provided a set of “state-of-the-art” potentials, from which reliable predictions can be made for other Rb isotopes. In particular, we have identified selected hyperfine states that provide large elastic cross sections, small inelastic cross sections, and novel quantum effects (i.e., interferences and resonances). These states offer prospects not only for interesting collision studies but also for unique degenerate gas experiments, involving both bosons and fermions. This is the subject of Sections 5.3 and 5.4.

5.1 Suppressed ^{87}Rb inelastic cross sections

Myatt, **et al.** measured[100] an inelastic spin exchange rate L_2 of $2.2(9) \times 10^{-14}$ cm^3/sec in collisions between the $|2, 2\rangle$ and $|1, -1\rangle$ hyperfine states of ^{87}Rb . At the time of the experiment, the triplet scattering length was estimated[102] to be 110 ± 10 a.u., whereas the singlet scattering length was completely unknown. Figure 5.1 shows the rate constant (using $a_t = 110$ a.u.) versus an assumed singlet scattering length a_s . It is immediately apparent that the measured value of L_2 places strict limits on a_s . After the published uncertainties in a_t were incorporated into our analysis, we reported[103] bounds on the singlet scattering length of $72 \leq a_s \leq 102$ (in a.u.).

We can interpret the strong suppression of spin-exchange collisions very simply within the energy-independent frame transformation approximation. First, the structure of the s -wave Hamiltonian in the coupled hyperfine representation (neglecting magnetic dipole and external magnetic field interactions) is as follows (see Fig. 5.2): the collision complex consists of six channels, three of which ($f(f_a, f_b) = 1(1, 2)$, $f = 3(1, 2)$, and $f = 4(2, 2)$), have purely triplet character at small R . The remaining three channels constitute an $f = 2$ spin-exchange coupled block. The zero-field inelastic processes are controlled to a large extent by this $f = 2$ Hamiltonian, which consists of one singlet and two triplet channels with one channel converging asymptotically to each of the hyperfine split thresholds (see Fig. 2.1). (Most inelastic spin-exchange processes for the bosonic isotopes are controlled by a similar three channel Hamiltonian, see Table 5.1). The symmetrized short-range reaction matrix for this $f=2$ Hamiltonian can be written in the FT limit (Eq. 4.39) as:

$$K^{\text{sr}} = \begin{pmatrix} 0.1875\bar{\tau}_s + 0.8125\bar{\tau}_t & 0.2652(\bar{\tau}_s - \bar{\tau}_t) & 0.2864(\bar{\tau}_s - \bar{\tau}_t) \\ 0.2652(\bar{\tau}_s - \bar{\tau}_t) & 0.3750\bar{\tau}_s + 0.6250\bar{\tau}_t & 0.4050(\bar{\tau}_s - \bar{\tau}_t) \\ 0.2864(\bar{\tau}_s - \bar{\tau}_t) & 0.4050(\bar{\tau}_s - \bar{\tau}_t) & 0.4375\bar{\tau}_s + 0.5625\bar{\tau}_t \end{pmatrix} \quad (5.1)$$

and $\bar{\tau}_\lambda = \tan \pi \mu_\lambda$. (The channel labels for K^{sr} are $1 \equiv (f_a, f_b f) = (11)2$, $2 \equiv (12)2$, and $3 \equiv (22)2$). The coefficients of the recoupling matrix (see Eq. 2.63)

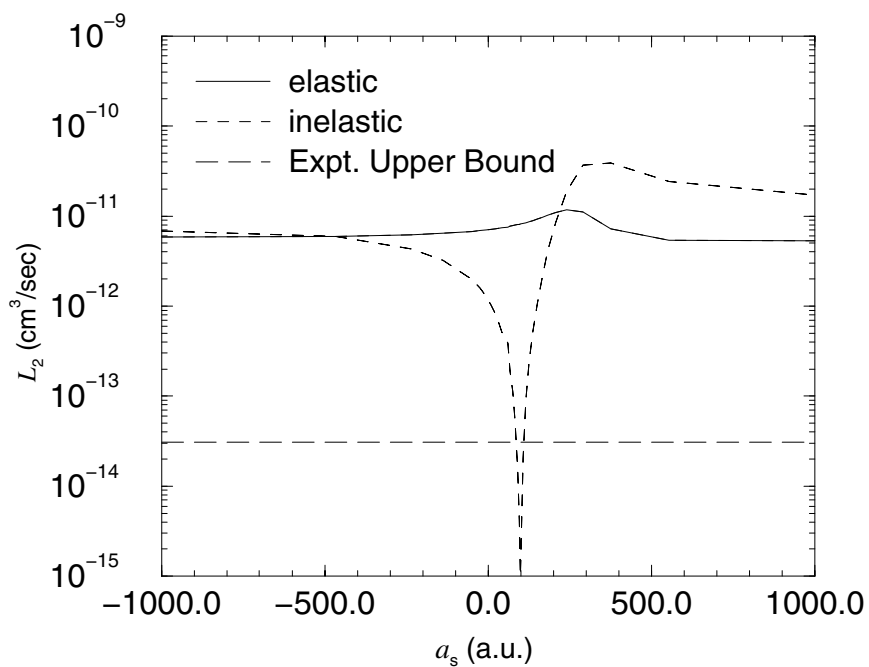


Figure 5.1: Elastic and inelastic event rates L_2 for the collision of $|2, 2\rangle_{87} + |1, -1\rangle_{87}$ atoms versus an assumed singlet scattering length a_s . The calculation is for an incident energy of $1\mu\text{K}$ above threshold with a fixed triplet scattering length of 110 a.u. The upper bound of the measured value $L_2 = 2.2(9) \times 10^{-14}$ cm³/sec is also displayed.

have been evaluated explicitly to show its structure. However, the transformation between spin representations is unitary and therefore the off-diagonal structure (i.e., proportional to $(\bar{\tau}_s - \bar{\tau}_t)$) is perfectly general for any coupled channel Hamiltonian in the FT limit. Evidently if the singlet (μ_s) and triplet quantum defects (μ_t) (or equivalently the two scattering lengths) are equal, then $\underline{K}^{\text{sr}}$ and also the \underline{S} matrix will be diagonal. In such a case the inelastic rates vanish.

Table 5.1: The zero-field Hamiltonian describing an unpolarized gas of identical bosons has a block diagonal structure in the coupled hyperfine representation (neglecting magnetic dipole effects). The total spin f labels and associated number of spin-exchange coupled channels are identified for the naturally abundant alkali isotopes. The single channel blocks are pure triplet channels. The two coupled channel block consists of a singlet and triplet channel converging to each of the two $f_a = f_b$ hyperfine thresholds. The three coupled channel block consists of one singlet and two triplet channels with one channel converging to each of the three hyperfine split thresholds (see Fig. 2.1).

Atom	Nuclear Spin	Single Channel	Two Channels	Three Channels
${}^7\text{Li}$	3/2	$f = 1,3,4$	$f = 0$	$f = 2$
${}^{23}\text{Na}$	3/2	$f = 1,3,4$	$f = 0$	$f = 2$
${}^{39}\text{K}$	3/2	$f = 1,3,4$	$f = 0$	$f = 2$
${}^{41}\text{K}$	3/2	$f = 1,3,4$	$f = 0$	$f = 2$
${}^{85}\text{Rb}$	5/2	$f = 1,3,5,6$	$f = 0$	$f = 2,4$
${}^{87}\text{Rb}$	3/2	$f = 1,3,4$	$f = 0$	$f = 2$
${}^{133}\text{Cs}$	7/2	$f = 1,3,5,7,8$	$f = 0$	$f = 2,4,6$

The physical picture is only slightly different from the FT approximation. Recall the discussion of spin-exchange in Section 3.3. There it was noted that the localization of the spin-exchange coupling at an internuclear separation of $R_I \sim 20 - 25$ a.u. presented an opportunity for interference. Physically, the incident wave splits when it propagates inward through the interaction region (R_I), sending amplitude into both singlet and triplet channels at short range. These wave components evolve nearly independently, reflect from their inner turning points, then recombine in the interaction region to produce the final mixture of exit channels. If the components meet with their original relative phase, the outgoing waves recombine constructively reproducing the original channel, in that case the scattering is primarily elastic. Otherwise, the amplitudes recombine destructively requiring scattering flux to exit in other channels. The suppression occurs when $a_s \sim a_t$ since singlet and triplet potentials quickly become degenerate for $R > R_I$, meaning that little additional phase difference accumulates. A similar interpretation emerges from the analysis of Dalgarno and Rudge[106]. This circumstance also explains the poor quantitative performance of the FT approximation in Fig. 4.11. The FT pre-

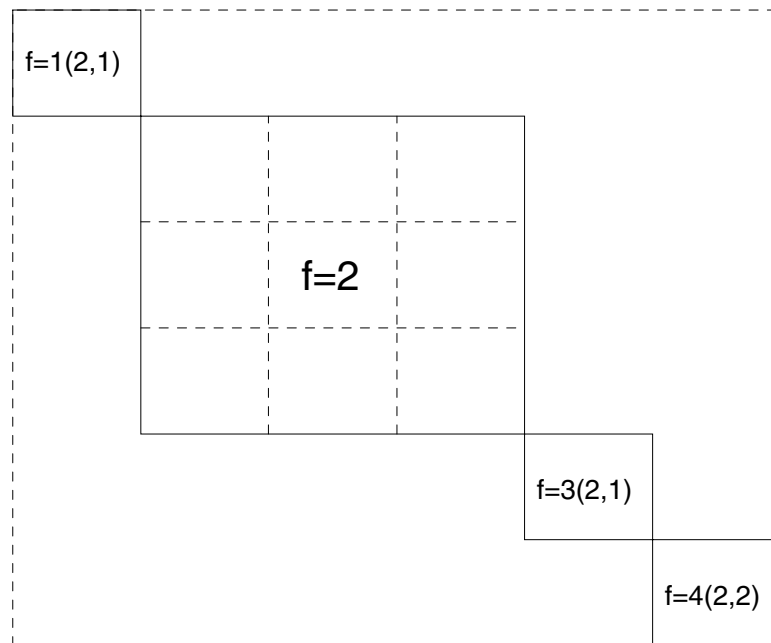


Figure 5.2: Block diagonal structure of the Hamiltonian describing the collision of $|2, 2\rangle_{87} + |1, -1\rangle_{87}$ atoms. The 6×6 Hamiltonian is presented in a coupled hyperfine representation with the nonzero matrix elements indicated by the corresponding $(f_a, f_b)f$ hyperfine labels. The $f=2$ block consists of three coupled channels.

dicts the suppression of the spin-exchange rates, but the suppression is erroneously predicted to be greatest when $a_s = a_t$ (see Fig. 5.3).

This interference picture can be further solidified by examining the singlet and triplet wave functions near R_I . Figure 5.4 shows zero-energy singlet and triplet wave functions. We see that the singlet wave function with $a_s = 99$ a.u. is very nearly in phase with the triplet, while that with $a_s = 553$ a.u. is out of phase. Changing the singlet scattering length from $-\infty$ to $+\infty$ introduces one additional node into the singlet wave function, pushing it through a π phase change in the interaction region. The result is one region of inelastic suppression per a_s cycle, as shown in Fig. 5.1.

However, if the collision complex contains asymptotically closed channels as is the case here, there is another interference mechanism that in principle can shut-off spin-exchange losses. As an example, consider the collision entrance channel to be the middle threshold (see Fig. 2.1) with one atom in its $f_a = 1$ hyperfine state and the other in its $f_b=2$ state (this is channel 2 in the above $\underline{K}^{\text{sr}}$, Eq. 5.1). In this case we must follow the procedure outlined in Section 4.2 to eliminate the asymptotically closed channel (channel 3). The new reaction matrix $\tilde{\underline{K}}$ is a 2×2 symmetric matrix with off-diagonal elements given by

$$\tilde{K}_{12} = K_{12}^{\text{sr}} - K_{13}^{\text{sr}}(\tan \beta(\varepsilon_3) + K_{33}^{\text{sr}})^{-1} K_{32}^{\text{sr}} . \quad (5.2)$$

If $\tilde{K}_{12} \rightarrow 0$ the resulting \underline{S} matrix is diagonal, again eliminating inelastic spin-exchange processes. Feynman path language can be used to interpret the above equation, where K_{ij}^{sr} is a measure of the flux transferred from channel j into channel i . The inelastic loss of atoms in our example can occur along one of two pathways; either flux is lost from channel 2 directly into channel 1, described by K_{12}^{sr} , or it is first transferred into the closed channel 3, evolves for awhile, and then hops from channel 3 into channel 1 and is lost, (described by the second term in Eq. 5.2). The two pathways can interfere, shutting off the inelastic processes. Inserting the FT matrix elements from Eq. 5.1, we find that $\tilde{K}_{12} \rightarrow 0$ when

$$\tan \beta(\varepsilon_3) = -\tan \pi \mu_t . \quad (5.3)$$

This relationship is general (within the FT approximation) for all three-channel Hamiltonians listed in Table 5.1. This example of spin-exchange suppression depends primarily on the triplet quantum defect (i.e., scattering length) and the threshold splitting (through the relationship $\varepsilon_3 = E - E_3$). It is therefore conceivable that a magnetic field could be employed to induce the interference, although a field necessarily complicates this simple analysis. Evidence for this type of magnetic-field induced interference will be provided in Section 5.3. Figure 5.5 shows the ^{87}Rb $f = (12)2$ inelastic rate over the entire $\mu_s - \mu_t$ plane. Here, we see the line of suppression along $\mu_s \sim \mu_t$ and also a horizontal line of suppression along $\mu_t = -\beta/\pi \sim 0.4$. The topology shown in Fig. 5.5 also was discussed within an

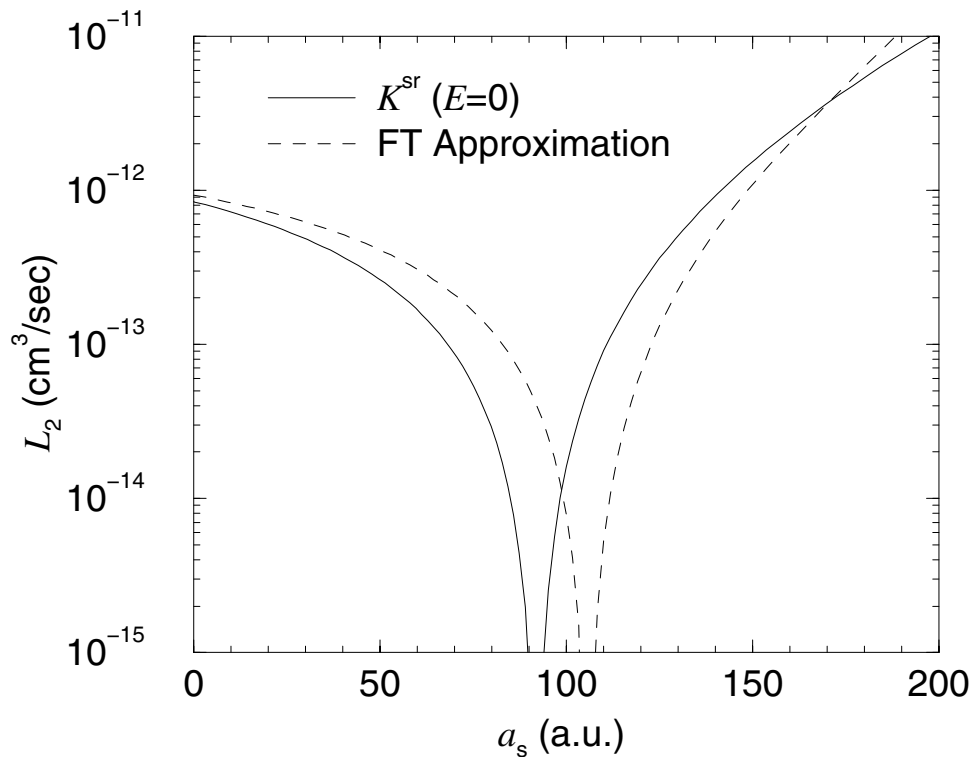


Figure 5.3: The inelastic rate constant L_2 is plotted versus an assumed singlet scattering length a_s . The FT approximation predicts $L_2 \rightarrow 0$ when $a_s = a_t$, here a_t is fixed at 106 a.u. However, the exact calculation predicts the minimum will occur at $a_s \simeq 92$ a.u. Our current best estimate of the ^{87}Rb singlet scattering length is 90 ± 1 a.u. The FT provides a poor approximation for ^{87}Rb inelastic rates, misrepresenting the rate by orders of magnitude, because of this small shift in the minimum rate position.

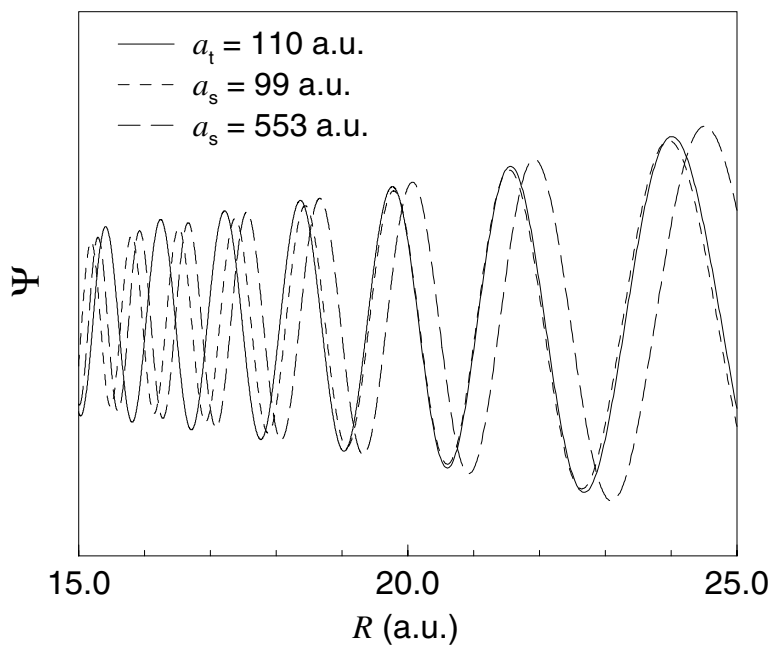


Figure 5.4: Zero-energy single channel wave functions for the singlet and triplet (solid line) Rb Born-Oppenheimer potentials as functions of the internuclear distance R . The singlet wave function is calculated assuming two different scattering lengths $a_s = 99$ and 553 a.u., while the triplet wave function corresponds to a scattering length of $a_t = 110$ a.u. The singlet ($a_s = 99$) and triplet wave functions are almost locked in phase through the region of large spin-exchange coupling ($R_I = 20-25$ a.u.) that accounts for the suppressed inelastic collisions.

adiabatic framework in Ref.[104].

5.2 Observation of a Feshbach resonance in ^{85}Rb collisions

A Feshbach resonance in the collision of two $|2, -2\rangle$ ^{85}Rb atoms, first predicted by Vogels, **et al.**[107], has now been observed independently by two groups[16, 17]. Using spectroscopic techniques, Ref.[16] detected the resonance through the magnetic field dependence of the photoassociation spectrum. Based on a theoretical analysis of the spectra, these authors reported the zero energy position of the resonance to be $B_{\text{max}} = 164 \pm 7$ G with a width of 8.2 ± 3.8 G. A more precise measurement was reported in Ref.[17]. Here, the technique of ‘‘cross-dimensional mixing’’[108] was employed. That is, the rf fields used for evaporative cooling quickly ‘‘chop-off’’ part of the atom cloud in a single dimension. The cloud equilibration time is directly related to the elastic collision rate. From these measurements, Roberts, **et al.** found the maximum and minimum collision rates occurred at field values of $B_{\text{max}} = 155.2 \pm 0.4$ G and $B_{\text{min}} = 166.8 \pm 0.3$ G.

The position of the resonance depends on both the singlet a_s and triplet a_t scattering lengths (or corresponding quantum defects) as well as the leading order dispersion coefficient C_6 . In addition, the width of the resonance reflects the coupling of bound and continuum channels and therefore provides an accurate measure of the scattering length difference $a_s - a_t$. We performed a parameter search over the singlet-triplet scattering length space for a number of dispersion coefficients. The phaseshifts generated by the Born-Oppenheimer potentials were adjusted by adding small corrections to their inner wall (Eq. 2.45) until the field values associated with the theoretical maximum and minimum of the thermally averaged elastic cross sections agreed with the measured B_{max} and B_{min} within experimental uncertainties. (The procedure for thermal averaging the rates and cross sections is presented in Appendix C.) An example of the allowed $\mu_s - \mu_t$ parameter space for a given $C_6 = 4700$ a.u. is provided in Fig. 5.6. As can be seen from this figure, the small measured uncertainties of B_{max} and B_{min} tightly constrain the allowed quantum defect ranges. In addition, we found that the area of this allowed parameter region was independent of the dispersion coefficients. Varying these coefficients simply shifted the region in $\mu_s - \mu_t$ space. To bound the parameter space completely, we required that our parameters also reproduced the measured g -wave shape resonance[102] within experimental uncertainties, which limits the van der Waals coefficient to $C_6 = 4700 \pm 50$. This value for C_6 is slightly larger but with smaller uncertainty than the most recently published value[109] of 4550 ± 100 a.u. We were unable to obtain useful limits on C_8 and C_{10} due to their small influence on the positions of both the shape resonance and the Feshbach resonance. Our final scattering length bounds were first reported[17] in terms of a fractional bound state phase ν to facilitate comparisons with Ref.[16]’s analysis. Here, the results are presented in terms of scattering lengths and corresponding quantum defects (see table 5.2). The final bounds on the

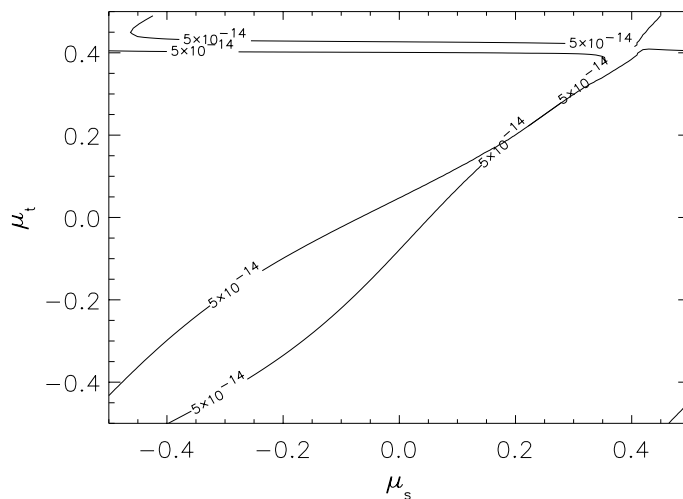


Figure 5.5: Inelastic collision rate L_2 for the process $f = 2(12) \rightarrow f = 2(11)$ in ^{87}Rb . The rates are plotted versus singlet μ_s and triplet μ_t quantum defects. The region of suppressed inelastic collisions are contained within the marked contour lines. These regions are discussed in the text. The physical values of the ^{87}Rb quantum defects are $\mu_s = -0.294$ and $\mu_t = -0.354$.

triplet quantities also include a ± 1 uncertainty[107] in the number of bound states supported by the Born-Oppenheimer potential.

As a further check of the resulting potentials, we confirmed that they predict scattering quantities that are consistent with previous measurements. In particular, our triplet potential supports a ^{87}Rb d -wave shape resonance[101]. The predicted ^{87}Rb $a_{2,1}/a_{1,-1}$ scattering length ratio[110] and thermally averaged $|2, 2\rangle + |1, -1\rangle$ inelastic rate constant[100] also agree with their measured values. In addition, we find 10 of the 12 measured ^{85}Rb d -wave bound states[109] within the 2σ experimental uncertainties. The new potentials also permit us to predict additional ^{85}Rb Feshbach resonances: one at $B_{\text{max}} = 226.0 \pm 4.0$ G with a width of ~ 0.01 G, and another at $B_{\text{max}} = 535.5 \pm 4.0$ G with a width of 2.2 ± 0.2 G.

The Feshbach resonance suggests a way to evaporatively cool ^{85}Rb , which has proven difficult at zero-field. Initially, the poor $B = 0$ evaporative cooling observed experimentally was surprising since it was known that the scattering length was large ($a \sim -400$), implying a large elastic cross section ($\sigma = 8\pi a^2$) at threshold. However, the ^{85}Rb s -wave partial cross section suffers Ramsauer-Townsend[24] type minimum at low energies ($E \approx 375$ μK) (see Fig. 5.7). We can understand the presence of this zero by studying the energy dependence of the elastic phase shift δ_l . Levinson's theorem[24] states that the zero-energy phase shift $\delta_l(0) = N\pi$ where N is the number of l -wave bound states supported by the potential. In the limit of infinite collision energy the phase shift $\delta_l \xrightarrow{E \rightarrow \infty} 0$. Each partial cross section ($\sigma_l \propto \sin^2 \delta_l$) will therefore suffer at least $N-1$ zeros as a function of energy. However, at low energies the s -wave phase shift is related to the scattering length $\delta_{l=0} = -ka$. For negative scattering lengths, the phase shift rises initially and therefore incurs at least N zeros as a function of energy. Levinson's theorem holds strictly only for a single channel interaction. However, we find that the low-energy behavior of the phase shift for multichannel collisions obeys this trend as well. Exceptions to this rule could occur if resonances are present in the relevant energy range.

The energy position of the first s -wave zero in a single channel interaction can be estimated using quantum defect theory. The physical phase shift is given in terms of our standardized quantum defect parameters by

$$\delta(E) = \tan^{-1} \left[\frac{A(E) \tan \pi \mu}{1 + \mathcal{G}(E) \tan \pi \mu} \right] + \eta(E). \quad (5.4)$$

For a given value of μ (which can be approximated as energy-independent in Rb up to about $E = 0.1$ K), this equation can be inverted to find the energy at which the physical phase shift obtains a specified value. In Fig. 5.8, the lines of constant $\delta = \pi/2$ (i.e., unitarity limit) and $\delta = 0$ are shown as a function of the quantum defect μ and the standardization parameter $\gamma^{1/4} = (2\mu C_6)^{1/4} k$, where $k = (2\mu E)^{1/2}$. This figure shows that the first zero in the s -wave partial cross-section will occur at lower energies for a negative scattering length than for a positive one. This does not turn

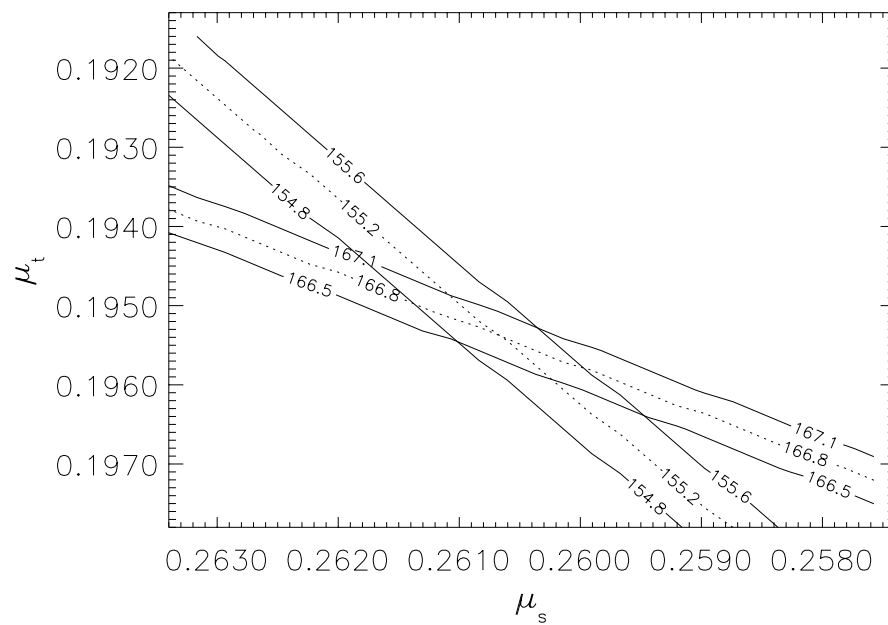


Figure 5.6: Lines of constant maximum $\sigma(B_{\max})$ and minimum $\sigma(B_{\min})$ cross section versus magnetic field are shown in singlet-triplet quantum defect space. The magnetic field values are labeled on each line, (dashed=nominal, solid=bounds). Dispersion coefficient values of $C_6=4700$, $C_8=523070$, and $C_{10} = 7665(10^4)$, in a.u., were used for this particular calculation.

Table 5.2: Singlet and triplet scattering lengths a (in a.u.) and quantum defects $\bar{\mu}$ (dimensionless) for the different Rb isotopic pairs given a constant $C_6 = 4700$ a.u. and $C_8 = 550600$ a.u. The uncertainty in the singlet quantum defect $\bar{\mu}_s$ is 0.0014 in all cases. Variations of the scattering lengths with C_6 and C_8 can be determined by the following formulas: $\mu = \bar{\mu} + b_6(C_6 - 4700) - b_8(C_8 - 550600)$ and $a = -C^2 \tan(\pi\mu)/(1 + \mathcal{G}(0) \tan(\pi\mu))$. Here, $C^2 = 0.957217(2mC_6)^{1/4}$, m is the reduced mass of the atom-pair (in a.u.), and $\mathcal{G}(0) = -1.0026$. The constant b_6 equals 7.5×10^{-5} for the singlet and 1.4×10^{-4} for the triplet. The constant b_8 is the same for both potentials and is given by 2.0×10^{-8} .

Pair	a_s	$\bar{\mu}_s$	a_t	$\bar{\mu}_t$
82-82	-38 ± 1	0.0612	$+151 \pm 10$	-0.491 ± 0.019
83-83	$+66 \pm 1$	-0.2021	$+81 \pm 3$	-0.262 ± 0.013
84-84	$+142 \pm 1$	-0.4678	$+15 \pm 3$	-0.033 ± 0.007
85-85	$+2400^{+600}_{-350}$	0.2603	-369 ± 16	0.194 ± 0.001
86-86	$+7 \pm 1$	-0.0144	$+211 \pm 7$	0.421 ± 0.007
87-87	$+90 \pm 1$	-0.2939	$+106 \pm 4$	-0.354 ± 0.003
82-87	$+55 \pm 1$	-0.1568	-40 ± 4	0.064 ± 0.004
83-87	-990^{+60}_{-70}	0.2263	-295 ± 7	0.184 ± 0.001
84-87	$+117 \pm 1$	-0.3952	$+550^{+45}_{-35}$	0.302 ± 0.004
85-87	$+11 \pm 1$	-0.0233	$+213 \pm 7$	0.418 ± 0.007
86-87	$+336 \pm 4$	0.3443	$+143 \pm 4$	-0.467 ± 0.010

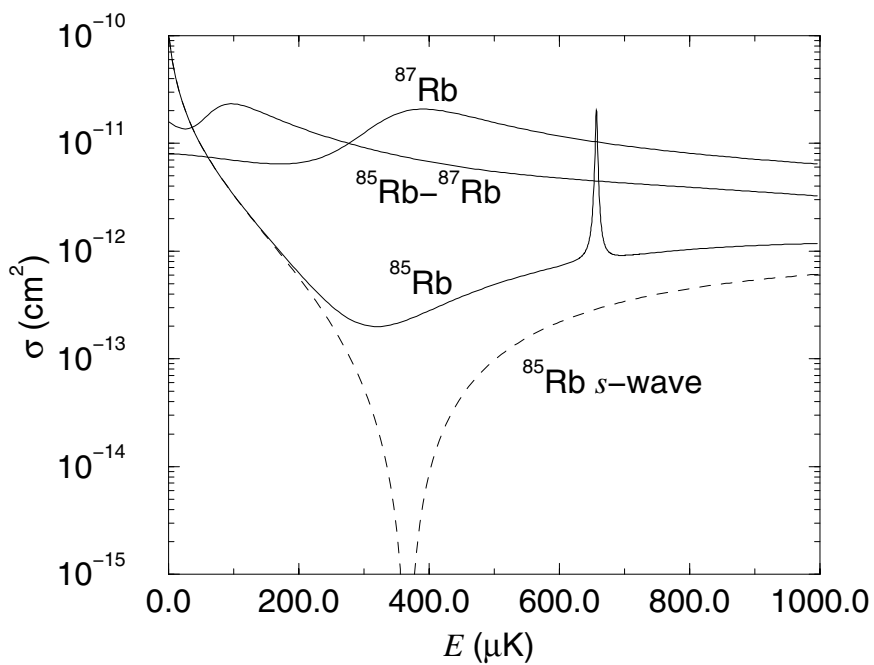


Figure 5.7: Total elastic cross sections for doubly polarized Rb collisions are plotted versus collision energy. The ^{85}Rb s -wave partial cross section suffers a minimum at $E = 375 \mu\text{K}$. In addition, a g -wave shape resonance ($E = 650 \mu\text{K}$) is evident in the ^{85}Rb total cross section. The ^{87}Rb cross section exhibits a broad d -wave shape resonance near $E = 400 \mu\text{K}$ and a p -wave shape resonance ($E \approx 100 \mu\text{K}$) enhances the mixed-isotope cross section.

out to be a problem for ${}^7\text{Li}$ ($a_t = -27.6$) simply because of its small mass. There, the first s -wave zero does not occur until $E > 1$ mK, well beyond the temperature range where evaporative cooling techniques are employed.

Evaporative cooling near a Feshbach resonance must tread a fine line, balancing increased inelastic as well as elastic collision rates. Although zero-field magnetic dipole loss rates for collisions occurring at the lowest hyperfine threshold are exceedingly small ($\sim 10^{-18}$ cm³/sec in Rb), near a resonance these rates can increase dramatically. The field-dependence of the ${}^{85}\text{Rb}$ $|2, -2\rangle$ dipole loss rate L_2 is shown in Fig. 5.9. At the measured resonance field value ($B_{\text{max}} = 155$ G) L_2 peaks at a loss rate of 10^{-13} cm³/sec. However, the peak loss rate is extremely energy-dependent, growing prohibitively large at energies below $1\mu\text{K}$. The good news is that the lineshape is asymmetric, with the minimum loss occurring on the positive scattering length side of the resonance. (Negative scattering length ramifications for a ${}^{85}\text{Rb}$ condensate are discussed at the end of Section 5.3.) It therefore looks promising for evaporative cooling to work if the bias field is set in the range $B \sim 160$ - 165 G. The dipole loss rates also show much more structure than the elastic rates. The broad resonances at $B > 300$ G are associated with d -wave spin-exchange coupled channels. A measurement of this structure could provide even tighter constraints on the Rb potentials than we have to date.

5.3 Predictions for ${}^{85}\text{Rb}$ - ${}^{87}\text{Rb}$ collisions

A second possible way to Bose-condense ${}^{85}\text{Rb}$ is to cool it sympathetically in a gas of ${}^{87}\text{Rb}$ atoms. The ${}^{85}\text{Rb}$ - ${}^{87}\text{Rb}$ triplet scattering length is large and positive (~ 200 a.u., see table 5.2) implying a large elastic collision rate between the atoms (see Fig.5.7). Generally, collisions between upper and lower manifold hyperfine states suffer large spin-exchange losses. (Note, however, the exception presented in Section 5.1.) Therefore, the two best choices for mixed-isotope condensation require trapping $|3, 3\rangle_{85}$ atoms with $|2, 2\rangle_{87}$ or trapping $|2, -2\rangle_{85}$ with $|1, -1\rangle_{87}$ atoms, as neither combination suffers spin-exchange losses. Of these two candidates, the second is the more interesting because the scattering length between isotopes can be “tuned” via Feshbach resonances. In principle, this should allow control of the overlap between the two condensates and produce **interpenetrating** quantum fluids. In this section, I provide updated values for the mixed-isotope scattering observables that were first reported in Ref.[111], reflecting our improved knowledge of the Born-Oppenheimer potentials.

The scattering length a for $|2, -2\rangle_{85} + |1, -1\rangle_{87}$ collisions in a magnetic field is shown in Fig. 5.10. Two pronounced resonances are apparent at field values of $B_{\text{max}} = 288.5 \pm 15$ and 420 ± 35 G with widths of 4 ± 1 and 47 ± 10 G, respectively. The energy-field evolution of these resonances is shown in Fig. 5.11. Here, the time delay operator[27] $Q = 2d\delta/dE$ is introduced. The signature of a resonance is a rapid increase by π radians in the physical phase shift δ . Therefore,

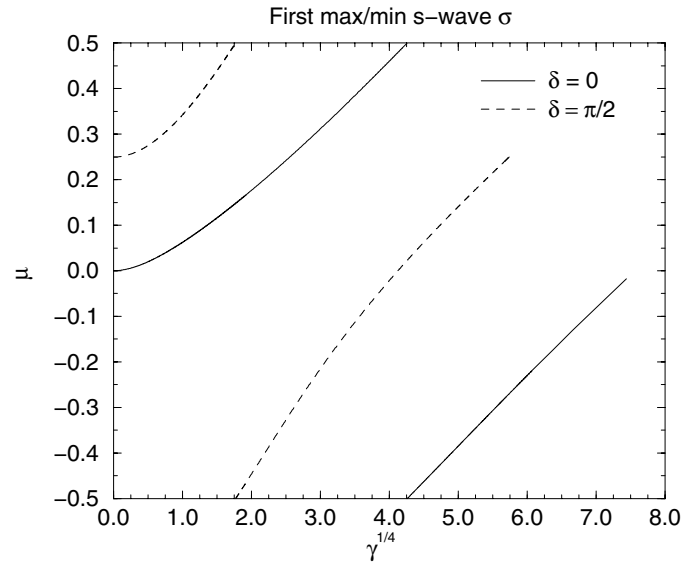


Figure 5.8: Constant lines of the physical s -wave phase shift δ are plotted versus quantum defect μ and the standardization parameter $\gamma^{1/4} = (2\mu C_6)^{1/4}k$, in a.u.. Negative scattering lengths correlate with $0 < \mu \lesssim 0.25$ (see Eq. 4.42). This figure shows that atom-pairs with negative scattering lengths suffer a zero in the s -wave cross-section at lower energies than positive scattering length pairs. Also, the unitarity limit ($\delta = \pi/2$) is obtained at lower energies for positive scattering lengths. The physical ^{85}Rb triplet quantum defect is 0.194. From this graph one finds the first zero occurs at roughly $\gamma^{1/4} = 2.2$ that is an energy of $366 \mu\text{K}$, in good agreement with the full calculation shown in Fig. 5.7.

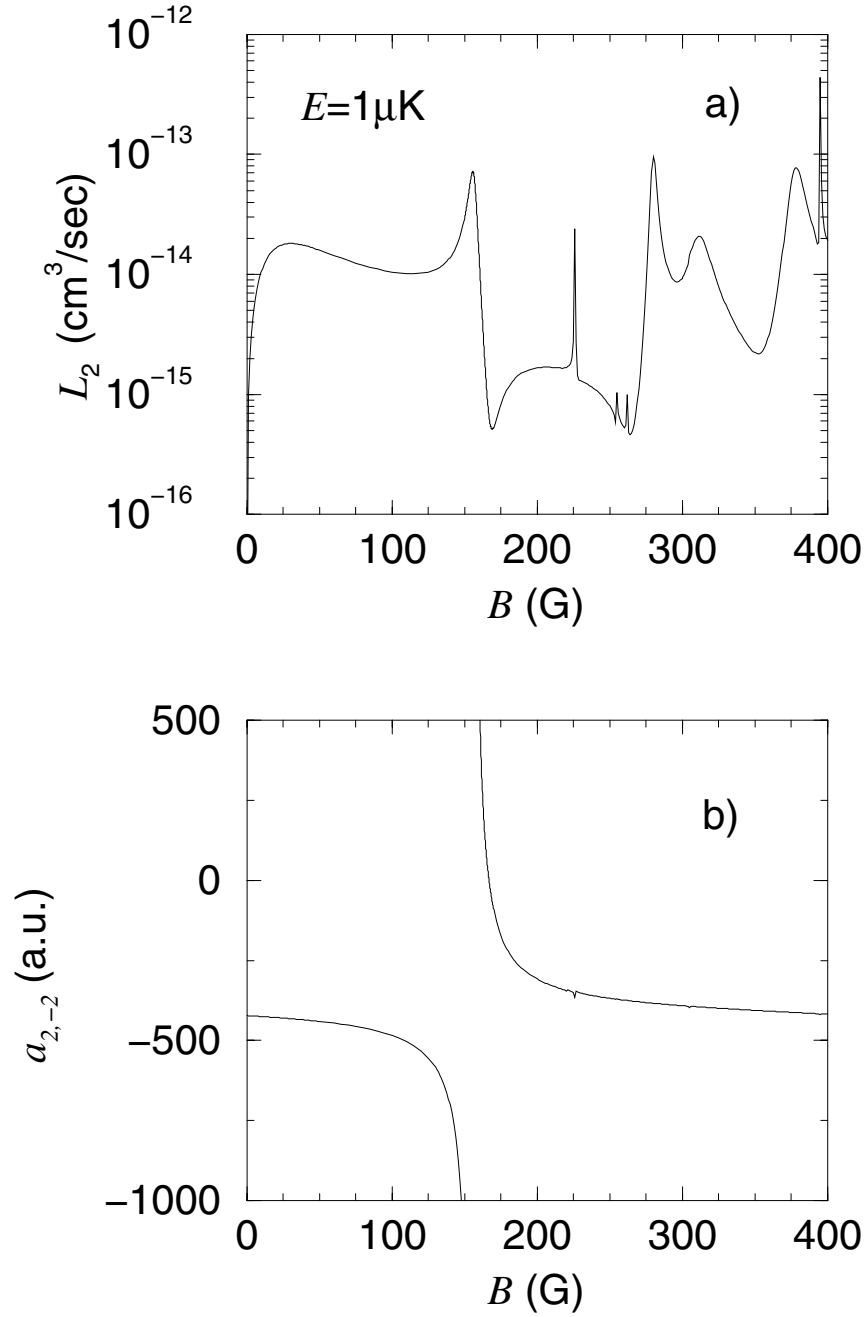


Figure 5.9: a) Magnetic field dependence of the inelastic dipole loss rate L_2 for collisions of two ^{85}Rb atoms in their $|2, -2\rangle$ hyperfine state and b) the corresponding scattering length dependence $a_{2,-2}$. The dipole loss rates exhibit a large increase at the measured Feshbach resonance ($B = 155$ G) field. The sharp feature in a) at $B \sim 225$ G is the narrow Feshbach resonance predicted previously. The broad features in a) $B > 300$ G are resonances in d -wave spin-exchanged coupled channels.

near a resonance, Q can be fit to a Lorentzian profile

$$Q = \frac{\Delta/2}{(E - E_r)^2 + (\Delta/2)^2}, \quad (5.5)$$

from which the maximum value Q_{\max} immediately identifies the width $\Delta = 2/Q_{\max}$ and resonance position E_r . It is sometimes useful to define a similar operator with respect to the change in field strength $Q_B = 2d\delta/dB$. (This analogous “time-delay” like definition of resonance position and width is not generally used for magnetic field resonances in the cold collision community. Instead, the resonance position is defined as the field B_{\max} at which $a(B_{\max}) \rightarrow \infty$ and the width is given by $\Delta = |B_{\max} - B_{\min}|$ where $a(B_{\min})=0$ (see Eq. 2.2.4). Positions and widths quoted in this work (including the ones given in this section) will adhere to these commonly accepted definitions unless otherwise stated.) The Feshbach resonances originate from $f=3$ and $f=4$ quasi-bound states that are nearly degenerate at zero field. The block diagonal structure of the 8×8 Hamiltonian that describes the s -wave collision complex is provided in Fig. 5.12. In zero-field, the $f = 3$ entrance channel is uncoupled from the $f=4$ spin-exchange coupled channels and therefore only one resonance appears in Fig. 5.11. As the bias field is turned on, the $f=4$ resonance immediately appears with an extremely narrow width “on top” of the $f=3$ resonance. As the coupling (H_B) is increased, the two states repel one another, eventually becoming completely separated in energy before crossing the entrance channel threshold. In addition the $f=4$ resonance broadens considerably as the coupling strength is increased.

Another interesting magnetic-field dependence is exhibited in the spin-exchange loss rates of $|3, 3\rangle_{85} + |1, -1\rangle_{87}$ collisions. Ordinarily, these two hyperfine-states would quickly expel one another from the trap due to their large spin-exchange rate, $L_2 = 3.4(10^{-12}) \text{ cm}^3/\text{sec}$. However, this rate turns out to be nonresonantly suppressed in the presence of a magnetic field. The field dependence of L_2 is shown in Fig. 5.13. The minimum rate of $\sim 10^{-15}$ occurs at $B = 297.5 \text{ G}$. A 12×12 Hamiltonian, with five channels open at $R \rightarrow \infty$, describes these s -wave collisions. It is therefore surprising (and nontrivial to explain) how an interference effect can shut down all four inelastic channels at the same value of the magnetic field. MQDT can be used to gain some insight into the dynamics. Figure 5.14 shows the short-range reaction matrix elements between the inelastic channels (labeled j) and the entrance channel (labeled 5), both before (K_{j5}^{sr}) and after (\tilde{K}_{j5}) eliminating closed channels. The elements of K_{j5}^{sr} are nonzero and almost constant in field. However, when the closed channels are eliminated from the reaction matrix all off-diagonal elements of \tilde{K}_{j5} go to zero over the same small range of magnetic field. Therefore, the closed-pathways are interfering with the direct paths in much the same fashion as discussed at the end of Section 5.1. The loss rate L_2 does not exactly vanish since the off-diagonal elements vanish at slightly different field strengths. This destruc-

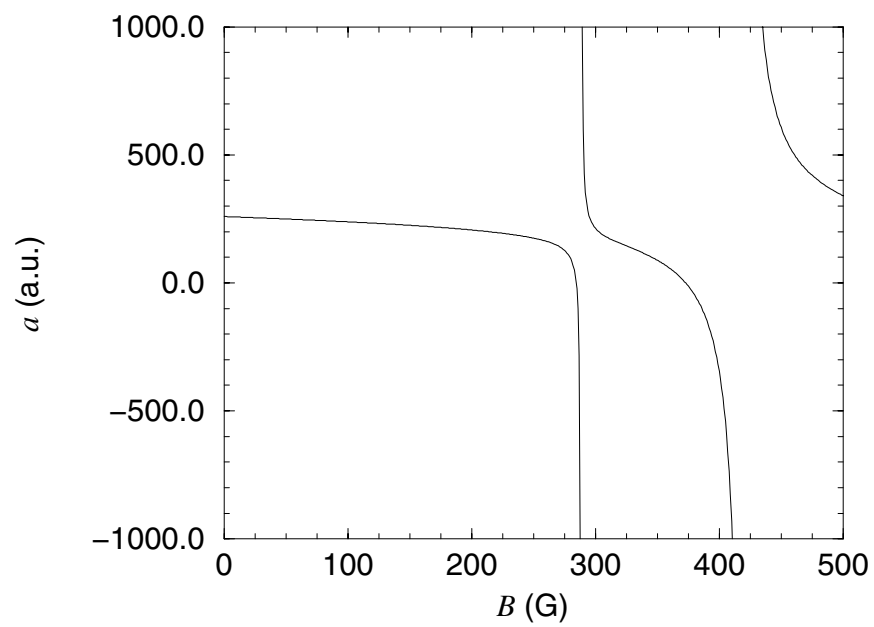


Figure 5.10: The magnetic-field dependence of the $|2, -2\rangle_{85} + |1, -1\rangle_{87}$ scattering length. The zero-energy position of the Feshbach resonances are 287.5 ± 15 and 420 ± 35 G with widths of 4 ± 1 and 47 ± 10 G, respectively.

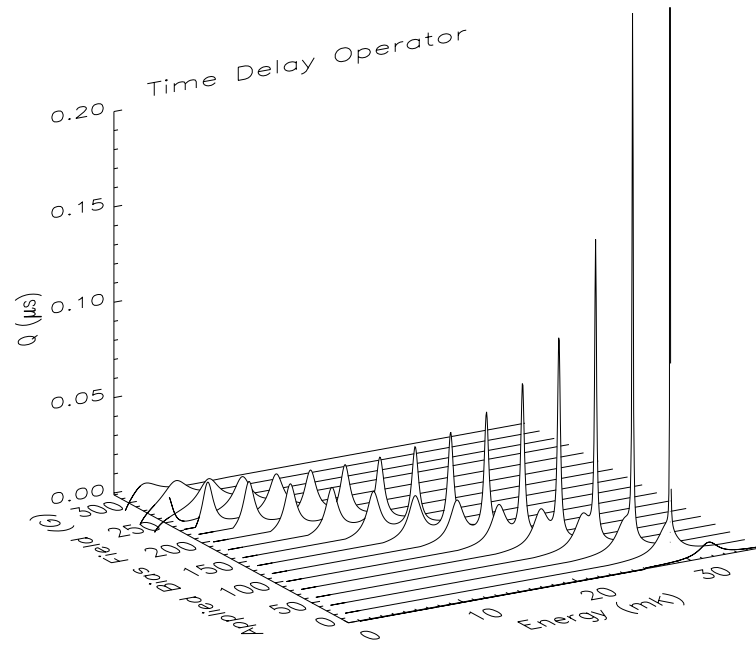


Figure 5.11: The evolution of two Feshbach resonances in energy and field are shown for collisions of $|2, -2\rangle_{85}$ and $|1, -1\rangle_{87}$ atoms. The time delay operator is defined as $Q = 2d\delta/dE$. Its peak value identifies the position and width $\Delta = 2/Q_{\text{max}}$ of each resonance.

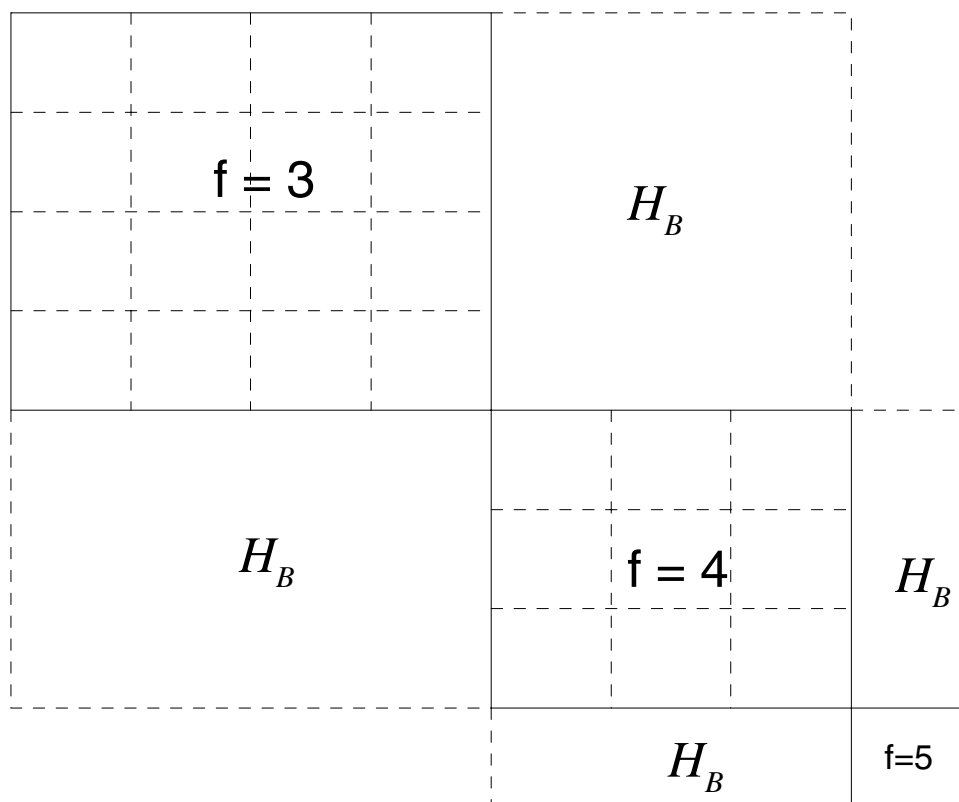


Figure 5.12: Block diagonal structure of the $|2, -2\rangle_{85} + |1, -1\rangle_{87}$ s -wave Hamiltonian. The $f=3$ spin-exchange coupled channels consist of 1 singlet and 3 triplet channels with one channel converging to each of the four hyperfine-split thresholds (see Fig. 2.1). The $f=4$ block consists of three channels, 1 singlet and 2 triplets, with one channel converging to each of the three highest energy hyperfine thresholds. The last $f=5$ block is a single triplet channel converging to the 3+2 hyperfine threshold. A magnetic field H_B introduces additional coupling within each spin-exchange block and couples the $\Delta f = \pm 1$ channels.

tive interference raises the possibility that a triple condensate could be formed in a magnetic trap with the species $|1, -1\rangle_{87}$, $|2, 2\rangle_{87}$, and $|3, 3\rangle_{85}$. Triple condensates of ^{23}Na atoms in each Zeeman sublevel of the $f_a=1$ hyperfine state have been observed in an all optical dipole trap[112].

A mixture of ^{85}Rb atoms and ^{87}Rb atoms exhibits interesting cold collision properties. However, this system suffers a drawback from the point of view of condensate mixtures. Namely, the large negative scattering length of ^{85}Rb implies that its condensate is unstable at $B = 0$ beyond ~ 100 atoms. The ^{85}Rb Feshbach resonance can in principle alter this situation by applying a bias field to tune its scattering length to a positive value, which should then allow large number condensates to be formed. Unfortunately, the ^{85}Rb scattering length is negative at the fields required to tune the 85-87 interaction. Therefore, experiments designed to exploit the 85-87 interaction must account for the small ^{85}Rb condensates. Detecting and studying such small condensates will be no small feat but may be possible[113].

5.4 Scattering properties of the short-lived Rb isotopes

Experimentalists have recently developed the ability to cool and trap short-lived radioisotopes. Experiments with francium[114, 115], sodium[116], as well as ^{82}Rb [117] have been reported. These experiments open up new territory, offering the possibility that these short-lived species can be used in studies of degenerate Fermi and Bose gases. In this section, I highlight some of the interesting scattering properties of the Rb radioisotopes. In particular, mixed isotope collisions of ^{83}Rb - ^{87}Rb and mixed spin state collisions of the individual fermionic isotopes ^{84}Rb and ^{86}Rb will be investigated. We first reported these results in Ref.[118]. That work showed that the ^{82}Rb scattering properties are only marginally suitable, at best, for degenerate gas studies and will not be discussed here.

First, consider the scattering properties of the fermionic isotopes. One of the most important considerations for degenerate gas studies is the magnitude of the elastic scattering cross section that enables evaporative cooling. The Pauli exclusion principle prohibits s -wave collisions between identical spin-polarized fermions. Therefore, formation of a degenerate Fermi gas will require sympathetic cooling of the atoms, by using either a different spin state or else a completely different atom. Both ^{84}Rb and ^{86}Rb are ideal candidates for sympathetic cooling with ^{87}Rb , since they have large positive triplet scattering lengths (see Table 5.2). In addition, they both have an ‘‘inverted’’ hyperfine structure, making $f = 5/2$ the lower energy state. (The atomic properties of the Rb isotopes considered here are provided in table 5.3.) This means that spin exchange losses are forbidden in collisions between $|5/2, 5/2\rangle_A$ and $|5/2, 3/2\rangle_A$ atoms, where $A = 84$ or 86 . Evaporative cooling of like-fermions in different spin states has been demonstrated[119] in ^{40}K , which has a similarly inverted hyperfine structure. However, the scattering length is negative for both 84-84 and 86-86 collisions, despite the positive sign of the singlet and triplet

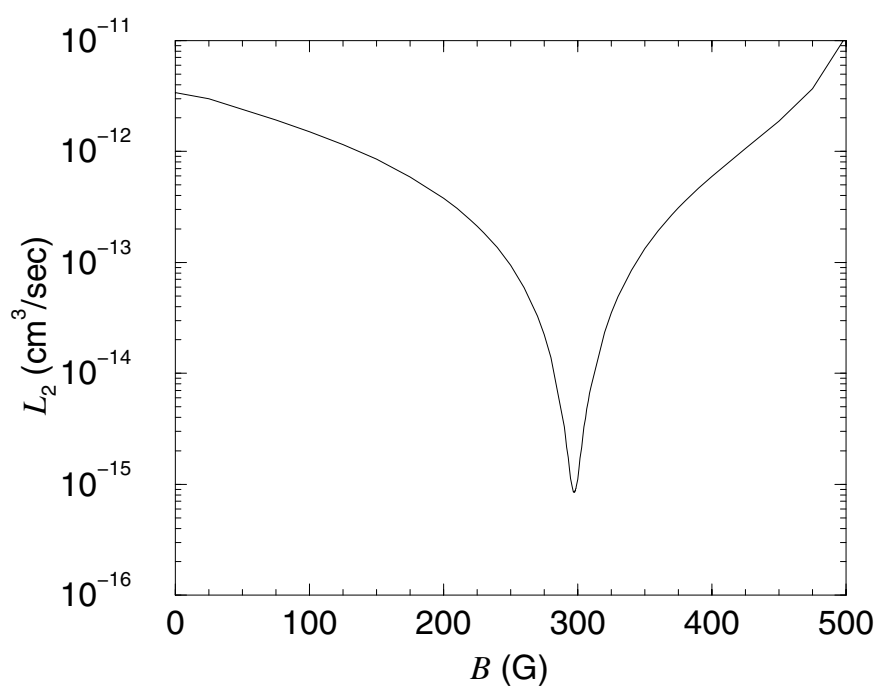


Figure 5.13: Field-dependence of the $|3, 3\rangle_{85} + |1, -1\rangle_{87}$ spin-exchange loss rate L_2 is plotted. A nonresonant suppression of the loss rate is observed at 297.5 ± 40 G.

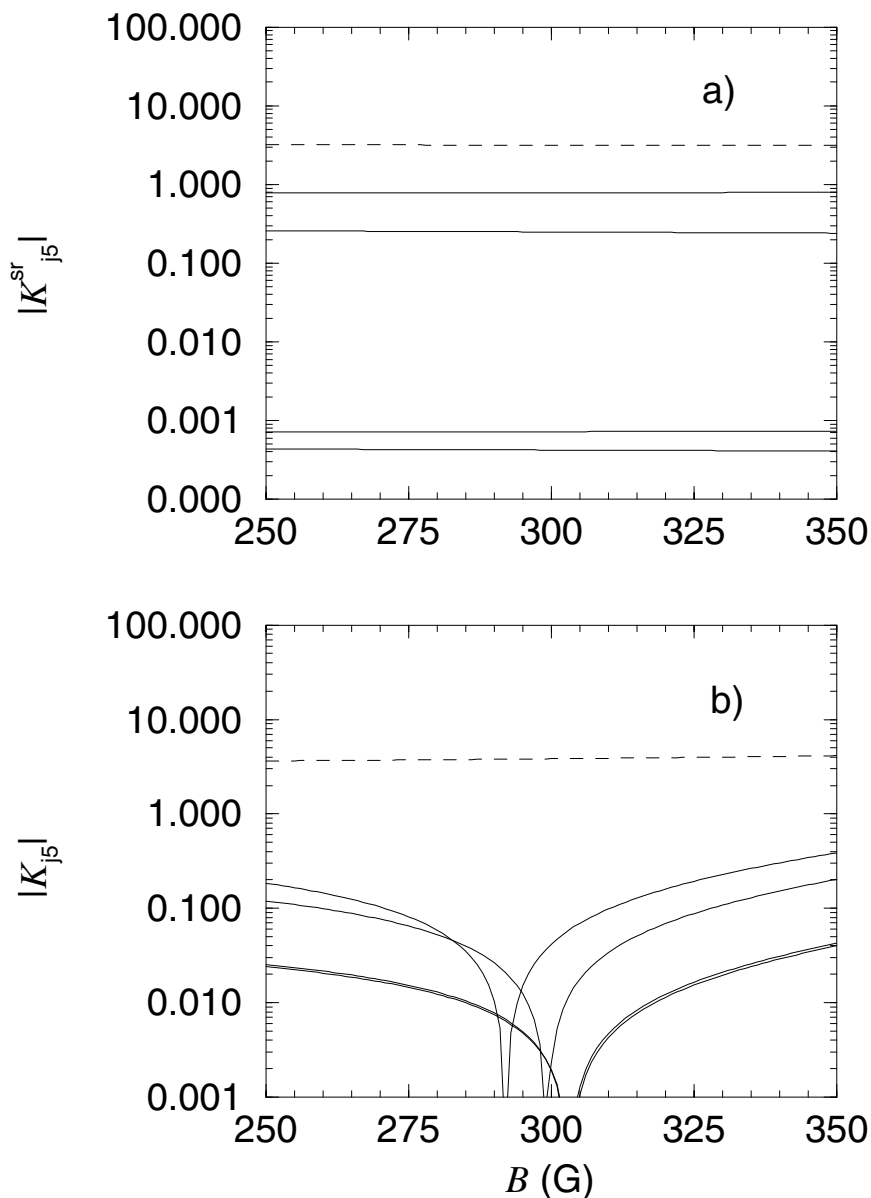


Figure 5.14: Field-dependence of the reaction matrix elements are plotted for collisions of $|3, 3\rangle_{85} + |1, -1\rangle_{87}$ atoms. In a) the elements of \underline{K}^{sr} that connect the entrance channel (labeled 5) to the inelastic channels are shown as solid lines and the diagonal element K_{55}^{sr} is represented by a dashed line. In b) the closed channels have been eliminated from \underline{K}^{sr} (Eq. 4.25). The elements of the new reaction matrix \tilde{K}_{j5} are plotted here. (solid = off-diagonal elements, dashed = diagonal element). The destructive interference between the direct and closed inelastic pathways is evident in Fig. b)

scattering lengths (see Table 5.2). Such a result, contrary to the ‘‘Degenerate Internal States’’ (DIS) model of hyperfine state scattering [106], bears exploring here.

Table 5.3: Nuclear spin I , ground-state atomic hyperfine splittings Δ , and half-life τ of the Rb isotopes. A negative value of Δ indicates an ‘‘inverted’’ hyperfine structure. The half-life units are m=minutes, d=days, y=years.

Isotope	I	Δ (GHz)	τ
82	1	1.5474	1.273 m
83	5/2	6.3702	86.2 d
84	2	-3.08316	32.9 d
85	5/2	3.03573	stable
86	2	-3.94688	18.63 d
87	3/2	6.83468	4.88(10 ¹⁰) y

If the magnetic dipole coupled channels are neglected, this is a coupled two channel problem with the $|5/2, 5/2\rangle_A + |3/2, 3/2\rangle_A$ channel energetically closed at $R \rightarrow \infty$. The unitary frame transformation connecting the short range basis with the uncoupled hyperfine basis implies that the entrance channel has 80 per cent triplet character. The DIS model, which neglects hyperfine energies, would then predict ($a = 0.8a_t + 0.2a_s$), i.e., that the 84-84 and 86-86 scattering lengths are both reasonably large and positive.

In fact, the positions of bound states relative to the appropriate hyperfine thresholds are crucial for determining the actual scattering length. We can explore the present situation by introducing a mixing angle θ to represent the coupling in this system[24]. The model for our potential is then

$$\underline{V} = \underline{U}(\theta)\underline{V}^S\underline{U}^T(\theta) + \underline{E} \quad (5.6)$$

where $\underline{U}(\theta)$ is a standard 2×2 real orthogonal rotation matrix, \underline{V}^S is a diagonal matrix of singlet and triplet Born-Oppenheimer potentials, and \underline{E} is a diagonal matrix of hyperfine energies. The model in the uncoupled limit ($\theta=0$) gives simply a triplet potential connected to the lowest hyperfine threshold (i.e., the entrance channel) and a singlet channel with one additional unit of hyperfine energy.

The θ -dependences of the ^{84}Rb - ^{84}Rb and ^{86}Rb - ^{86}Rb bound states are shown in Fig. 5.15. In ^{86}Rb (Fig. 5.15a), we find an extremely high-lying bound state in the uncoupled limit ($\theta=0$) that accounts for the large triplet scattering length. As the coupling is turned on, a nearly degenerate pair of bound states, one singlet and one triplet, begin to repel each other. Eventually the singlet state ‘‘pushes’’ the high-lying triplet state above threshold, resulting in a negative scattering length. In ^{84}Rb (Fig. 5.15b) the highest-lying bound state is rather deep ~ 100 MHz for $\theta = 0$, in accord with this isotope’s small positive triplet scattering length. As the coupling is turned

on, this bound state interacts with a “singlet” state lying above threshold pushing it still deeper into the potential, ultimately producing a negative scattering length. In both cases, the position of the singlet states relative to the **upper** hyperfine threshold are the determining factors in the physical scattering length.

Finally, we can compare the DIS scattering length result with that predicted by the frame transformation approximation. The short-range reaction matrix in the frame transformation approximation is given by

$$K^{\text{sr}} = \begin{pmatrix} 0.2\bar{\tau}_s + 0.8\bar{\tau}_t & 0.4(\bar{\tau}_s - \bar{\tau}_t) \\ 0.4(\bar{\tau}_s - \bar{\tau}_t) & 0.8\bar{\tau}_s + 0.2\bar{\tau}_t \end{pmatrix}. \quad (5.7)$$

Again, the notation $\bar{\tau}_\lambda = \tan \pi \mu_\lambda$ is used. Channel 2 is then eliminated (see Eq. 4.25) leaving a single elastic matrix element

$$\tilde{K}_{11} = K_{11}^{\text{sr}} + \frac{K_{12}^{\text{sr}} K_{21}^{\text{sr}}}{K_{11}^{\text{sr}} + \tan \beta(-\Delta)}. \quad (5.8)$$

The scattering length (Eq. 4.38) is given in terms of this matrix element by

$$a = \frac{-C^2 \tilde{K}_{11}}{1 + \mathcal{G}(0) \tilde{K}_{11}}. \quad (5.9)$$

Inserting values for the quantum defects (Table 5.2), the zero energy constants C^2 , $\mathcal{G}(0)$ (Table 4.1), and the phase parameter $\beta(\varepsilon = -\Delta)$ (a table of values for the long-range MQDT parameters is provided in Ref.[120]), the FT approximation predicts scattering lengths (in a.u.) of $a = -103$ and -286 for ^{84}Rb - ^{84}Rb and ^{86}Rb - ^{86}Rb , respectively. The frame transformation approximation reproduces the scattering lengths to within 20% of their physical values of $a = -115$ (^{84}Rb) and $a = -237$ (^{86}Rb), including the correct sign. The difference in the two models can be seen immediately from Eq. 5.8. In MQDT language, the DIS model is equivalent to setting $\tilde{K}_{11} = K_{11}^{\text{sr}}$, which completely neglects the influence of the closed channel. The closed-channel physics is crucial in this particular case and it is the inclusion of this physics that distinguishes the frame transformation approximation from the DIS model.

The (surprisingly) negative scattering length implies a net attraction between the two spin states $|5/2, 5/2\rangle_A + |5/2, 3/2\rangle_A$, which could have important consequences for forming Cooper pairs in these fermionic systems [121, 122]. On the other hand, the negative scattering lengths in these species again produce zeros in their s -wave cross sections, as shown in Fig. 5.16. The good news is that ^{84}Rb exhibits a Feshbach resonance in the presence of modest-sized magnetic fields (Fig. 5.17a). This resonance could then be used to move the position of the s -wave partial cross section zero to higher collision energies (Fig. 5.17b), allowing the atoms to be evaporatively cooled into the degenerate regime. The extremely large width of this

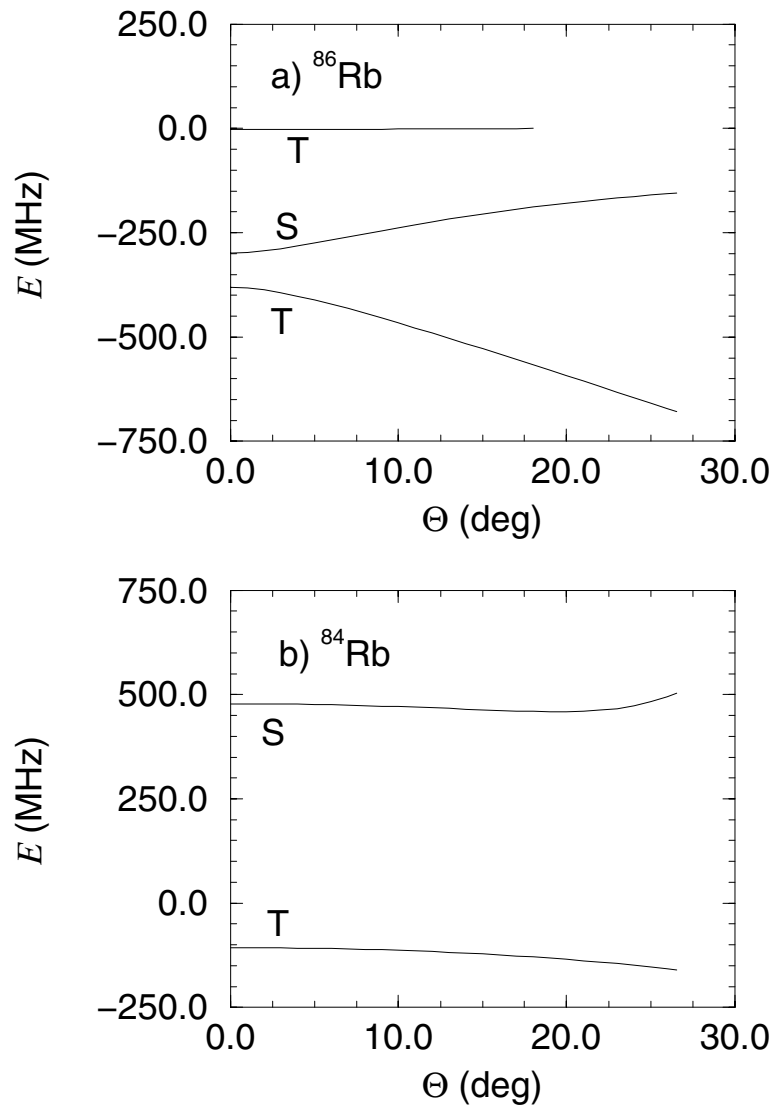


Figure 5.15: Bound and quasi-bound state positions versus the coupling parameter θ . The physical coupling strength is given by $\theta=26.57^\circ$. The labels S, T refer to singlet or triplet states in the $\theta = 0$ limit. Zero energy defines the entrance channel threshold.

a) $|5/2, 5/2\rangle_{86} + |5/2, 3/2\rangle_{86}$.

b) $|5/2, 5/2\rangle_{84} + |5/2, 3/2\rangle_{84}$.

resonance eliminates the need for accurate control of magnetic field strengths. The resonance would also allow the experimentalist a means to study both repulsive and attractive effective interactions between atoms in a single system.

In the ^{86}Rb case, a magnetic field will also influence the scattering length, but will change its sign only at very large fields ≈ 2800 gauss (Fig. 5.17a). The position of the cross section zero can be moved to a higher collision energy (Fig. 5.17b), but to a lesser extent than in ^{84}Rb . However, in this case the s -wave zero is not a major problem, since the enhanced p -wave scattering should enable the experimentalist to evaporatively cool the ^{86}Rb mixed spin states without a magnetic field bias. However, introducing a bias field of a few hundred gauss would increase the low energy total cross section by roughly a factor of 3.

Finally, consider the bosonic isotope ^{83}Rb . The singlet and triplet ^{83}Rb scattering lengths are relatively large, positive and very nearly the same (see table 5.2). These are remarkably similar to ^{87}Rb implying that ^{83}Rb by itself adds little to the field of BEC. However, mixtures of ^{83}Rb and ^{87}Rb atoms do offer some exciting possibilities. First, the ^{83}Rb - ^{87}Rb triplet scattering length is large and negative (see Table 5.2), which is not surprising since the ^{83}Rb - ^{87}Rb reduced mass is very nearly the same as two ^{85}Rb atoms. Therefore, a double condensate with large numbers of atoms could in principle be formed from the hyperfine states $|3, 3\rangle_{83} + |2, 2\rangle_{87}$. Within the Thomas-Fermi approximation, a double condensate composed of equal mass atoms with scattering lengths a_1 and a_2 is unstable whenever the mutual scattering length a_{12} satisfies $|a_{12}| > \sqrt{a_1 a_2}$ [123, 124]. This relationship is strictly true only for isotropic like-species condensates. However, a more general derivation[125] for anisotropic mixed-isotope double condensates shows that the instability remains. The nature of this instability has yet to be fully interpreted, particularly in the case of a_{12} negative. The 83-87 mixture would provide a good system to explore this phenomenon. In addition, Feshbach resonances arise in collisions between atoms in the lower hyperfine manifold (see Fig. 5.18), i.e. $|2, -2\rangle_{83} + |1, -1\rangle_{87}$. Thus, in contrast to the ^{85}Rb - ^{87}Rb system, it is possible to envision two large condensates with a tunable interspecies interaction. This capability could enable detailed studies of double condensates, all the way from completely overlapping to utterly immiscible[126, 127], in particular near the stability limits where $|a_{12}| \approx \sqrt{a_1 a_2}$.

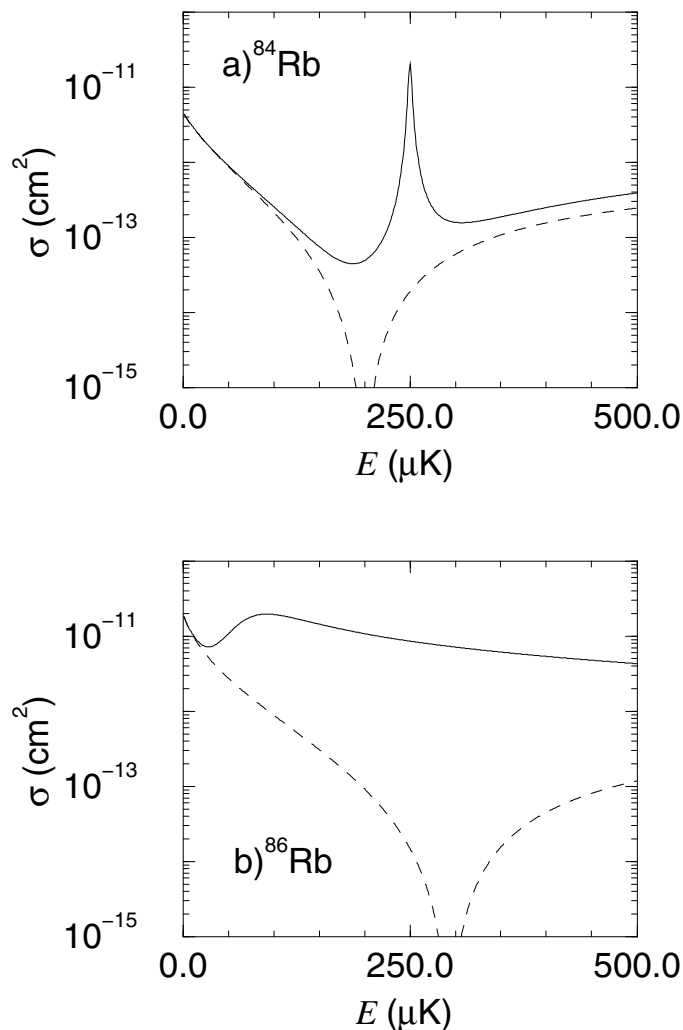


Figure 5.16: Elastic cross sections versus collision energy using our nominal potentials. Solid lines represent the total cross section, dashed lines indicate the s -wave contribution. The energy position of the first zero in the s -wave partial cross section is $200 \pm 30 \mu\text{K}$ for a) and $295 \pm 25 \mu\text{K}$ for case b).

a) $|5/2, 5/2\rangle_{84} + |5/2, 3/2\rangle_{84}$.

The feature near $250 \mu\text{K}$ in the total cross section is a f -wave shape resonance. Although we find the position of this resonance is uncertain to $\pm 150 \mu\text{K}$, it does not contribute over a broad enough energy range to compensate for the zero in the s -wave cross section.

b) $|5/2, 5/2\rangle_{86} + |5/2, 3/2\rangle_{86}$.

We find a broad p -wave shape resonance near $60 \mu\text{K}$. The height of the p -wave centrifugal barrier is roughly $80 \mu\text{K}$. In this case, the strong p -wave scattering is probably enough to compensate for the zero in the s -wave cross section.

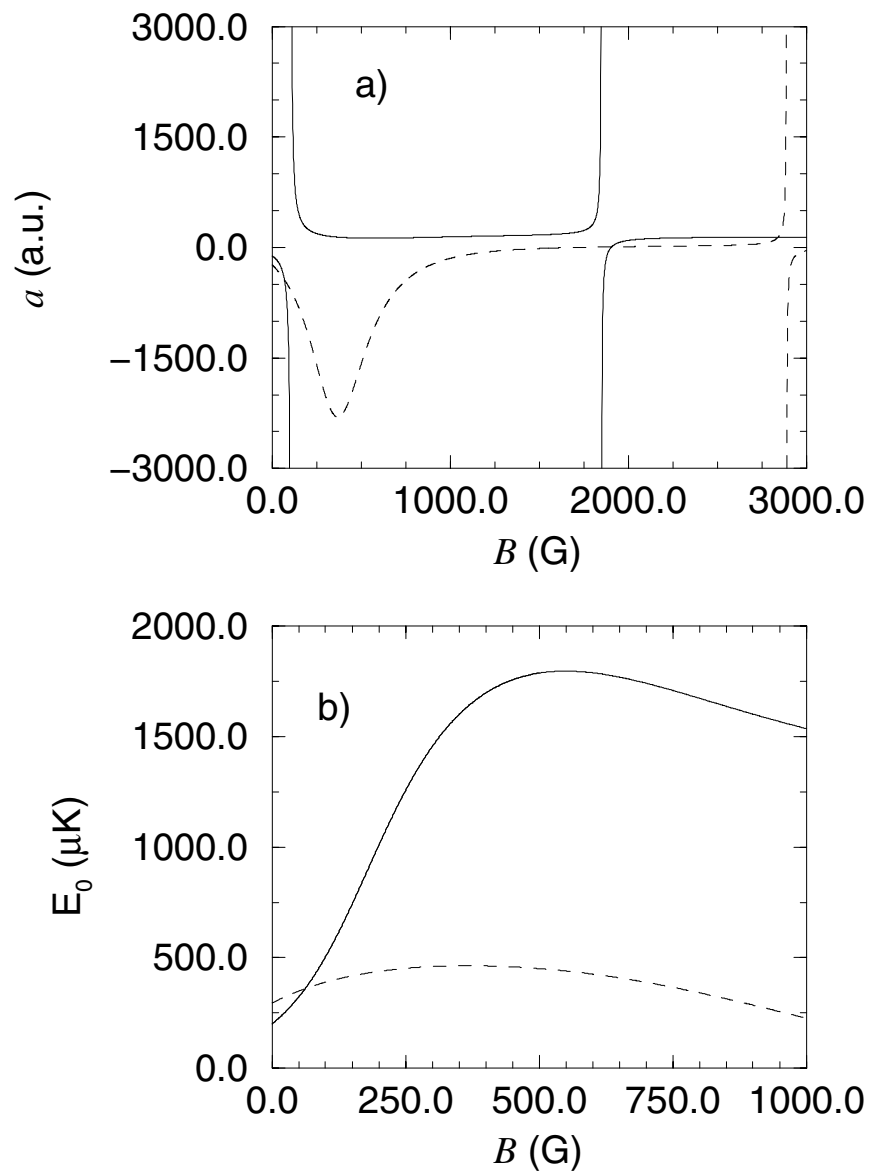


Figure 5.17: Solid lines represent $|5/2, 5/2\rangle_{84} + |5/2, 3/2\rangle_{84}$ collision, dashed lines represent the same spin state collision for ^{86}Rb .

a) Scattering lengths versus applied magnetic field. The zero energy positions of the low-field ^{84}Rb resonance is 106 ± 9 G.

b) Energy position E_0 of the first s -wave partial cross section zero versus applied magnetic field.

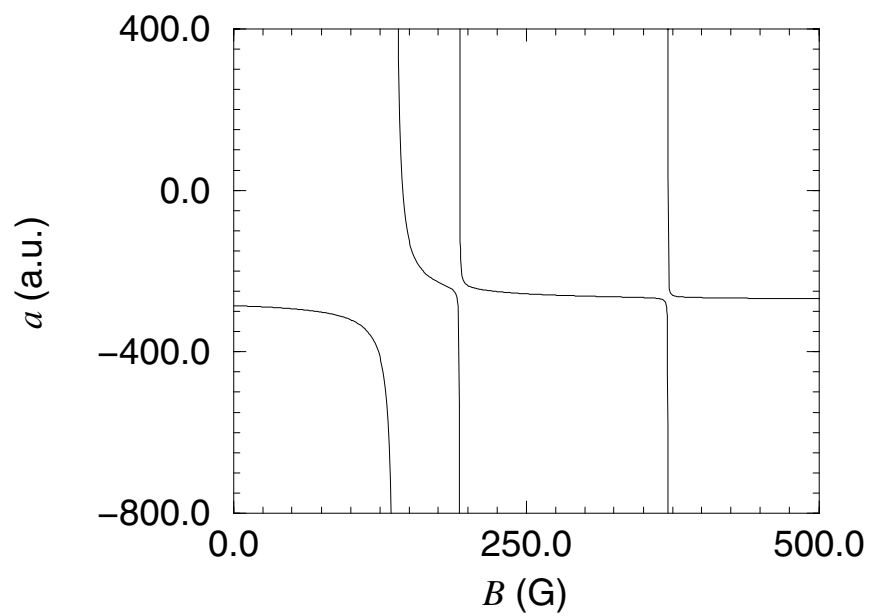


Figure 5.18: Scattering length versus applied magnetic field for a collision of $|2, -2\rangle_{83} + |1, -1\rangle_{87}$ atoms. The zero energy positions of the resonance peaks are 138 ± 10 G, 193 ± 8 G, and 371 ± 3 G. The low-field resonance has a width of $\Delta = 6.5 \pm 2.5$ G. The two higher field resonances are extremely narrow ($\Delta \ll 1$ G).